PCCP

Accepted Manuscript

ROYAL SOCIETY OF CHEMISTRY

www.rsc.org/pccp

RSCPublishing

ARTICLE

Multiple-state interfacial electron injection competes with excited state relaxation and deexcitation to determine external quantum efficiencies of organic dye-sensitized solar cells

Cite this: DOI: 10.1039/x0xx00000x

Received 00th January 2012,
Accepted 00th January 2012

DOI: 10.1039/x0xx00000x

www.rsc.org/

Min Zhang, Lin Yang, Cancan Yan, Wentao Ma and Peng Wang*

A comprehensive description of the complicated dynamics of excited state evolution and charge transfer at the photochemical interface in dye-sensitized solar cells is crucial to understand the mechanism of converting solar photons to clean electricity, laying an informative basis for the future development of advanced organic materials. By selecting two triarylamine-based organic donor–acceptor dyes characteristic of the respective benzoic acid and cyanoacrylic acid anchors, in this paper we reveal the picture of stepwise excited state relaxations and multiple-state electron injections at a realistic titania/dye/electrolyte interface based upon ultrafast spectroscopic measurements and theoretical simulations. Density functional theory (DFT) and time-dependent DFT calculations show that the optically generated "hot" excited state of dye molecules can undergo a significant conformational relaxation via multistage torsional motions, and thereby transform into an equilibrium quinonoid structure characteristic of a more planar conjugated backbone. A suit of kinetic parameters derived from the target analysis of femtosecond transient absorption spectra have been utilized to estimate the electron injection yield, which is in good accord with the maximum of external quantum efficiencies.

Introduction

Understanding the photoinduced interfacial electron transfer (ET) events is a theme of intense research in various fields of modern chemistry, such as photoelectrolysis, photocatalysis, and photovoltaic cells.[1–5] In this context, the titania/dye/electrolyte interface is a key part of the dye-sensitized solar cells (DSCs).[6] Thereby, snapshotting the dynamics of ET from the multiple excited states of a narrow energy-gap dye to the wide band-gap semiconductor is of vital importance for the future development of new materials and device engineering. During the past years, a large amount of research interest has been dedicated to tracing the ultrafast charge photogeneration kinetics in DSCs.[7–10]

It has been well documented in some literatures that electron injection from the "hot" excited state of a polypyridyl ruthenium dye can occur in the femtosecond time scale,[11–16] which is even considered to be the dominant ET process in view of a very strong interfacial electron coupling.[17,18] To a significant measure this notion has made people think little of the limitation of electron injection on the cell external quantum efficiencies (EQEs). However, more recent experiments have identified, in DSCs with a realistic electrolyte, the presence of multiexpotential electron injection kinetics even featuring a broad time range from femtoseconds to nanoseconds.[19–23] Note that most of the early ultrafast measurements were carried out in the absence of an electrolyte with some additives, which could significantly alter the interfacial energetics and electron injection kinetics.[24] Moreover, most of the kinetic measurements were recorded at a selected wavelength while the wavelength dependent kinetics were indeed been probed,[25] very likely owing to the presence of a severe signal overlap of excited states and charge separated states. We strongly suspect that some measured kinetic traces could be mainly ascribed to the excited state evolution.

Now it is widely accepted that the electron injection yield (ϕ_{ei}) in DSCs is virtually dependent of the kinetic competition between electron injection and excited state deactivation.[26] This cognition can be well demonstrated by some systems based upon small energy-gap organic dyes, which usually display low EQEs originated from the inferior ϕ_{ei}. The reduced driving force for electron injection and the short excited state lifetime of a narrow energy-gap organic dye may be two key factors. Nevertheless, less attention has been paid to a complete description of the intricate excited state evolution of organic donor–acceptor dyes and electron injections from the associated multiple excited states.[27–31]

Recently, by attaching the benzoic acid (BA) anchor to a chromophoric core of triphenylamine functionalized cyclopentadithiophene-benzothiadiazole (TPA-CPDT-BT, Fig. 1), we have developed an efficient organic dye (**C257**, Fig. 1).[32] However, this dye features a narrow spectral response to the

solar irradiance, limiting the photocurrent output. Thereby, we further replace the BA anchor of **C257** with a more electron-deficient cyanoacrylic acid (CA) anchor to construct a new dye (**C265**, Fig. 1) with a reduced energy-gap. In this contribution, with these two dyes in hand we attempt to make an in-depth scrutiny on the origins of dye structure dependent electron injection yields, which determine the maxima of EQEs. We lay special stress on the crucial role of excited state conformation relaxation in multiexpotential interfacial electron injection dynamics, based upon time-resolved spectroscopic measurements and theoretical simulations.

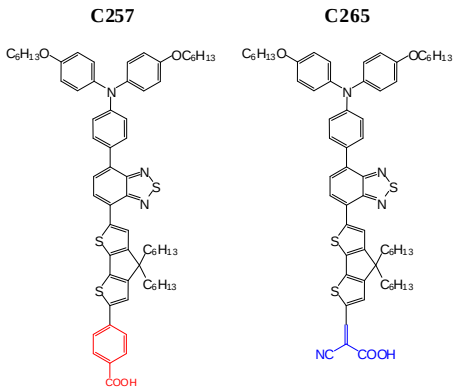

Fig. 1 Chemical structures of the two donor–acceptor dyes, **C257** and **C265** with the BA (red) and CA (blue) anchors, respectively. Herein, C_6H_{13} denotes the *n*-hexyl substituting group. The TPA-BT-CPDT chromophoric core is drawn in black.

Results and discussion

Both voltammetric measurements and theoretical calculations have shown that the replacement of BA with the more electron-deficient CA does not alter the highest occupied molecular orbital (HOMO) energy level too much, but brings forth a downwards displacement of the lowest unoccupied molecular orbital (LUMO) energy level. The resultant energy-gap shrinkage endows the **C265** dye dissolved in tetrahydrofuran with a red-shifted absorption peak in comparison with **C257**. For a detailed discussion, see ESI.† The reduced energy-gap, improved molar absorption coefficient, and increased dye loading amount (2.0×10^{-8} mol cm^{-2} μm^{-1} for **C265** and 1.8×10^{-8} mol cm^{-2} μm^{-1} for **C257**) jointly confer an augmented solar photon harnessing capacity on a dye-grafted mesoporous titania film, as presented in Fig. 2a. In combination with a conventional iodine electrolyte, we also employed the **C257** and **C265** grafted bilayer titania films to fabricate DSCs. The details for cell fabrication are described in the experimental section. As depicted in Fig. 2b, a perceptible bathochromic photocurrent onset wavelength can be noted upon the substitution of BA with CA. However, the **C265** cell exhibits a remarkably lower EQE summit of only 55%, in contrast to that of 88% for **C257**, albeit its saturated absorption in a broad visible spectral region (Fig. 2a).

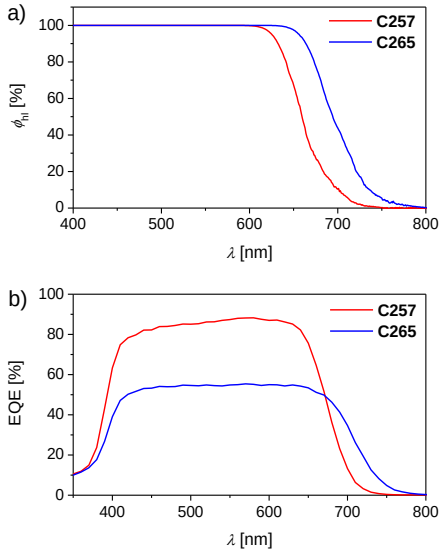

Fig. 2 (a) Plots of light harvesting efficiency (ϕ_{lh}) as a function of wavelength (λ) for a 9.0-μm-thick, dye-grafted mesoporous titania film immersed in an iodine electrolyte for DSC fabrication.(b) Plots of external quantum efficiency (EQE) as a function of wavelength (λ) for cells made with a dye-grafted bilayer (9.0+5.0-μm thick) titania film and an iodine electrolyte.

To understand the origins of significant EQE height variation, we measured the femtosecond transient absorption (fs-TA) spectra of the dye-grafted mesoporous titania films in contact with an iodine electrolyte (Figs. 3a and 3b) to elaborate the dynamics of excited state evolution and carrier photogeneration and furthermore to directly determine ϕ_{ei}. The very disparate kinetic traces presented in Figs. S4 and S6 of ESI have suggested that there could be a severe spectroscopic superposition of the ground state, excited state, and charge-separated state in the recorded fs-TA spectra (Figs. 3a and 3b). Obviously, we cannot evaluate electron injection kinetics by monitoring the signal at a selected wavelength in this spectral region. At the heterointerface of DSCs with donor–acceptor organic dyes, the light excitation promotes the dye molecules via intramolecular charge transfer to a non-equilibrium excited state, i.e. the Franck-Condon (FC) excited state. In the subsequent discussion we will call this "hot" state "CT_1" owing to its charge transfer character. CT_1 may undergo stepwise vibrational and torsional relaxations to form an equilibrium excited state.[33–35] During the relaxation, de-excitation to the ground state (GS) and charge separation via electron injection[26,36] from the excited dye molecules to titania can occur. By recording the static absorption and photoluminescence (PL) spectra of dye-grafted titania films (Fig. S8),† we have indeed found that there are large Stokes shifts of 0.62 eV for **C257** and 0.66 eV for **C265**. These large energy losses have somehow suggested the presence of significant excited state relaxations, probably owing to the change of excited state conformations.

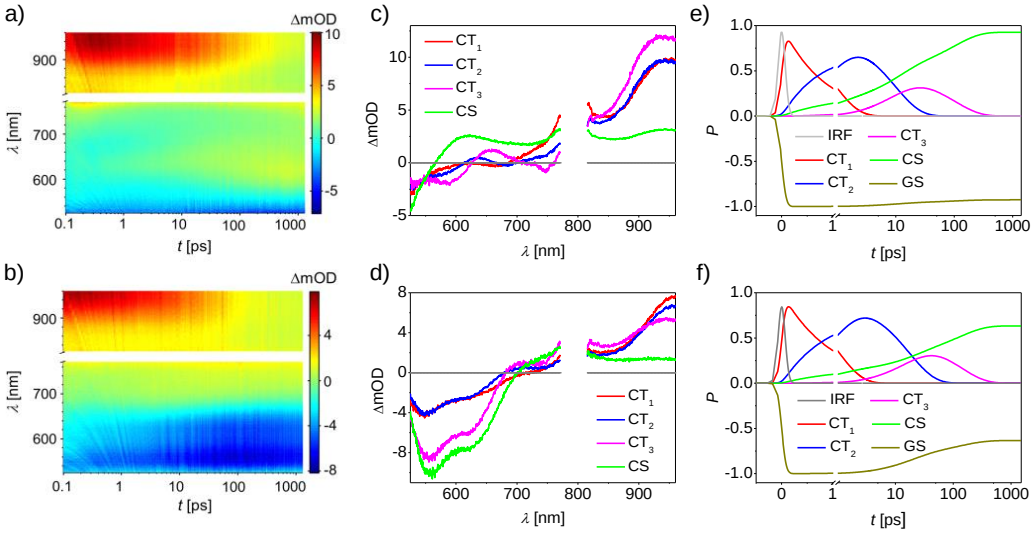

Fig. 3 (a, b) fs-TA spectra of 2.1-µm-thick, mesoporous titania films grafted with **C257** (panel a) and **C265** (panel b), which are also in contact with an iodine electrolyte. The pulse fluence of pump light at 490 nm is 13.9 uJ cm^{-2}. (c, d) Species-associated difference spectra of CT_1, CT_2, CT_3, and CS for the **C257** (panel c) and **C265** (panel d) samples, which are generated via target analysis of the spectra in panels a and b. (e, f) Kinetic traces generated by target analysis, for GS (dark yellow), CT_1 (red), CT_2 (blue), CT_3 (magenta), and CS (green) of the **C257** (panel e) and **C265** (panel f) samples. The grey lines in panels e and f represent the instrument response functions (IRF).

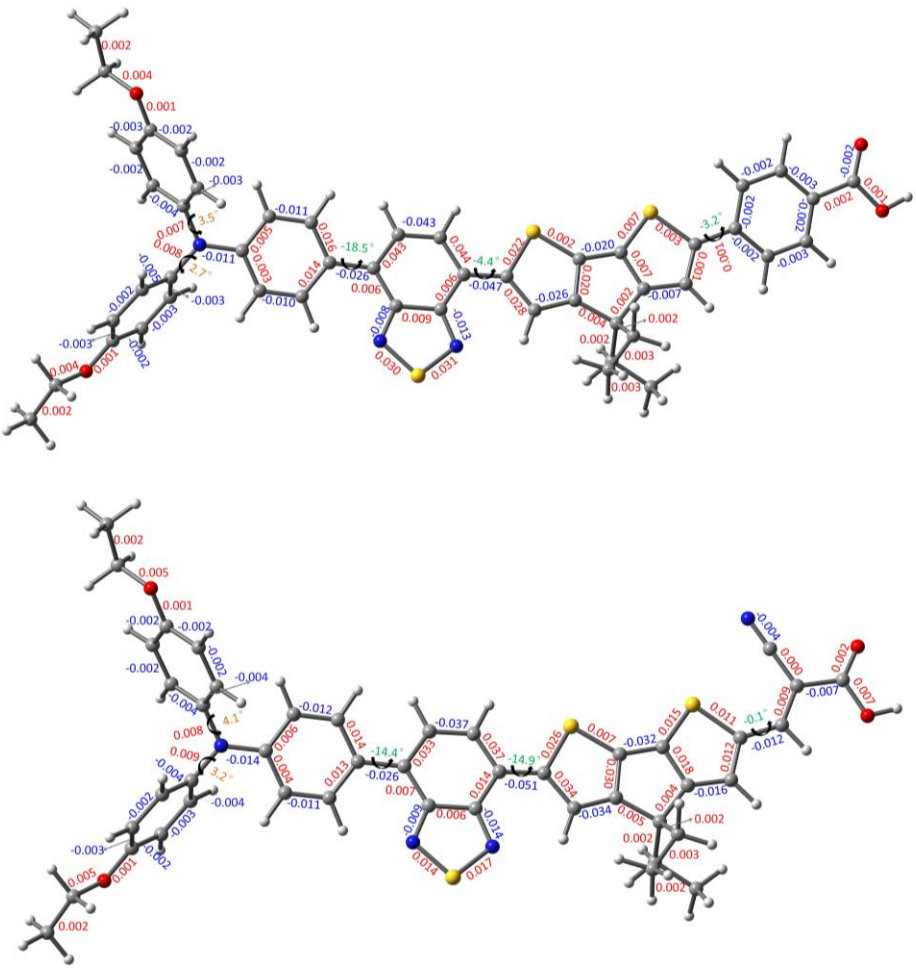

Fig. 4 Changes of bond length in angstroms (red and blue numbers) and dihedral angle in degrees (orange and green numbers) for **C257** (upper) and **C265** (lower) during the excited state relaxation from the optically generated "hot" excited state to the equilibrium excited state.

To get further insights into structural relaxation, the molecular geometries in the ground state (S_0) and the relaxed lowest singlet excited state (S_1) were optimized by resorting to the density functional theory (DFT) and time dependent density functional theory (TDDFT) calculations at the PBE0/6-311G(d,p) and TD-CAM-B3LYP/6-311G(d,p) levels, respectively. The exchange-correlation functional of CAM-B3LYP[37] is good at treating some excited states characteristic of long-range charge transfer,[38] which can also be demonstrated herein by comparing the calculated and measured maximum absorption wavelengths, maximum PL wavelengths, and Stokes shifts as listed in Table S2 of ESI.† Note that the optically generated "hot" excited state has the same geometry as S_0. Thereby, a marked conformational relaxation in the excited states can be perceived by looking at the optimized geometries of S_0 and S_1 (Fig. S9 and Fig. S10 of ESI).† Variations in bond length and dihedral angle can be found from Fig. 4. The dihedral angles of the two alkoxyl-substituted phenyl rings with respect to the benzothiadiazole attached phenyl unit become slightly larger. A length increase for the two C–N bonds in the alkoxyl-substituted diphenylamine (ADPA) segment is concomitant with a length decrease for the C–N bond connecting ADPA with the conjugated backbone. An evident planarization and a quinonoid character can be perceived for the conjugated backbones of **C257** and **C265**, which has also been noted for other organic conjugated materials.[39] Note that the optimization of both ground state and excited state structures with the CAM-B3LYP functional also give the same conclusion of torsional relaxation (see details from Fig. S11 and Fig. S12 in ESI).† In general, such torsional relaxations will cause stabilization of the lowest excited state.[40]

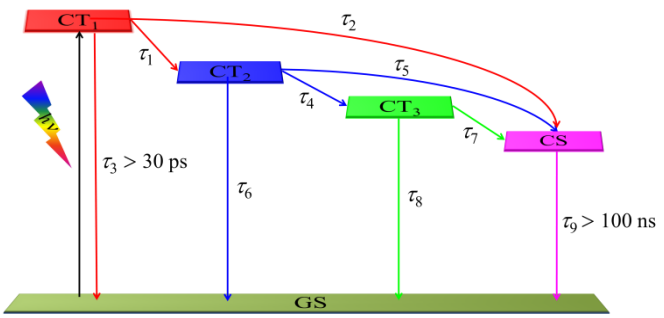

Scheme 1 The five-state dynamic model used in our target analysis of fs-TA spectra of organic dye-grafted titania films immersed in a realistic iodine electrolyte. Apart from the ground state (GS), four transient species at the titania/dye interface comprise three charge transfer states (CT_1, CT_2, and CT_3), and one charge separated state (CS). The "hot" CT_1 state is optically generated and can relax via torsional motions to form the CT_2 intermediate state and the CT_3 equilibrium state. τ_1 and τ_4 are the excited state relaxation time constants; τ_3, τ_6, and τ_8 are the deexcitation time constants; τ_2, τ_5, and τ_7 are the electron injection time constants.

On the basis of aforementioned knowledge, we thereby performed target analysis[41–43] by using a dynamic model of multiple-state electron injections as depicted in Scheme 1, and identified four key species, including CT_1, two stepwise relaxed charge transfer excited states (CT_2 and CT_3), and the charge separated state (CS). For the details on target analysis method, see ESI.† The time constants of species evolution derived from the target analysis were compiled in Table 1, which can be utilized to nicely reproduce the kinetic traces at a set of wavelengths (Figs. S4 and S6 of ESI) and the difference spectra at a suit of time delays (Figs. S5 and S7 of ESI).† The species-associated difference spectra (SADS) of the key components of CT_1, CT_2, CT_3, and CS were depicted in Figs. 3c and 3d. Their kinetic traces were presented in Figs. 3e and 3f.

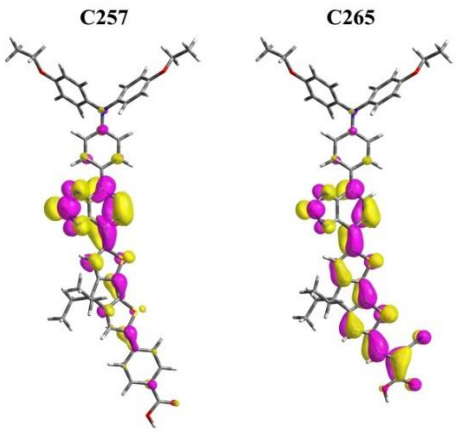

Fig. 5 The distribution of optically excited electrons in the "hot" excited states (CT_1) of **C257** and **C265**.

The **C265** dye possesses a time constant (τ_1) of 1.1 ps for the evolution from the "hot" CT_1 to the "partly relaxed" CT_2, very similar to that of 1.0 ps for **C257**. Also, no significant difference in the time constant (τ_2) of electron injection from the "hot" CT_1 has been probed for these two dyes (6.7 ps for **C265** and 4.7 ps for **C257**) albeit a ca. 230 meV difference between their LUMO energy levels. Also note that the dye transformation from **C257** to **C265** does not give rise to an obvious shift of the titania conduction-band edge, for details see the following discussion. Thereby the driving force insensitive kinetics of electron injection from CT_1 could be mainly ascribed to a strong electron coupling between CT_1 and titania for **C265**. This can be easily understood by taking a look at the LUMO distributions of their ground states, which we herein consider to be just the locations of optically excited electrons (Fig. 5) in the "hot" CT_1. The LUMO of **C257** is mainly localized on the benzothiadiazole unit which is far away from the surface of titania, while **C265** presents a broad LUMO distribution on the whole benzothiadiazole-cyclopentadithiophene-cyanoacrylic acid (BT-CPDT-CA) backbone. From our fittings, it can be noted that there is a negligible branching ratio for the deexcitation from CT_1 to the ground state (GS), in view of the distinctly larger time constants over 30 ps.

Moreover, although the **C265** dye displays a larger time constant (τ_4) of 36.3 ps for the subsequent relaxation from CT_2 to the equilibrium excited state (CT_3) with respect to that of 19.9 ps for **C257**, it has a more sluggish electron injection from CT_2 and an obviously shorter time constant of deexciation from CT_2 to GS (see Table 1 for details). The latter two factors dominate a lower branching ratio of electron injection from CT_2 for **C265**. It is noted that the time constants (τ_7) of electron

injection from CT_3 to titania are remarkably reduced compared to those from CT_1 and CT_2, being 109.6 ps for **C257** and 199.2 ps for **C265**. This can be ascribed to the large energy losses induced by the torsional motions, being 0.30 eV for **C257** and 0.32 eV for **C265** as derived from theoretical calculations on hot and equilibrium excited states. In addition, the **C265** dye presents an obviously slower electron injection from CT_3 and a significantly faster deexcitation from CT_3 to GS than **C257**, which jointly engender a lower branching ratio of electron injection from CT_3. Overall, the averaged time constants ($\tilde{\tau}_{ei}$) for the three-exponential generation of CS from CT_1, CT_2, and CT_3 are 49.5 ps for **C257** and 73.7 ps for **C265**. Furthermore, on the basis of the extracted time constants, we computed ϕ_{ei} to be 93% for the **C257** cell and 63% for the **C265** cell, via equation

$$\phi_{ei} = \tau_1/(\tau_1+\tau_2)+[\tau_2\tau_6/[(\tau_1+\tau_2)\times(\tau_4\tau_5+\tau_4\tau_6+\tau_5\tau_6)]]\times[\tau_4+\tau_5\tau_8/(\tau_7+\tau_8)] \quad ,$$

giving a distinct clue on the aforementioned dissimilarity of EQE maxima.

Table 1 Time constants derived from target analysis of fs-TA spectra of dye-grafted titania films immersed in a realistic iodine electrolyte

Dye	τ_1 [ps]	τ_2 [ps]	τ_3 [ps]	τ_4 [ps]	τ_5 [ps]	τ_6 [ps]	τ_7 [ps]	τ_8 [ps]	τ_9 [ps]	$\tilde{\tau}_{ei}$ [ps]
C257	1.0	4.7	>30	19.9	21.2	181.8	109.6	1386.2	$>10^5$	49.5
C265	1.1	6.7	>30	36.3	71.4	66.0	199.2	398.4	$>10^5$	73.7

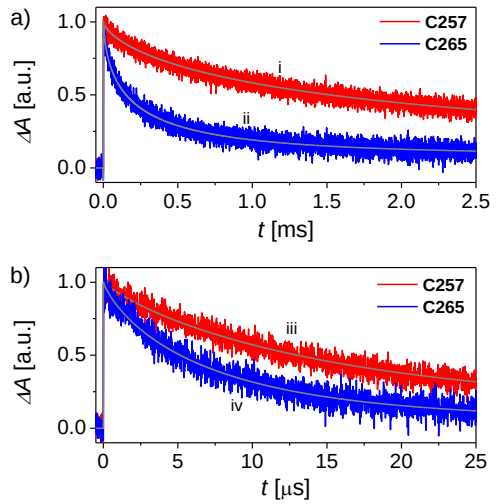

Fig. 6 Absorption traces at a probe wavelength of 785 nm upon 5 ns laser excitation for the 4.2-μm-thick, dye-grafted titania films immersed in the inert (panel a) and iodine (panel b) electrolytes. The pump wavelengths are selected in terms of a 0.4 optical density (OD) of the testing sample and the pulse fluence are precisely controlled to afford an analogous distribution profile of light excitation. Excitation wavelength and pulse fluence: 607 nm and 12 μJ cm^{-2} for curve i; 642 nm and 17 μJ cm^{-2} for curve ii; 611 nm and 12 μJ cm^{-2} for curve iii; 643 nm and 17 μJ cm^{-2} for curve iv. The grey lines are fittings to a stretched exponential function $\Delta A \propto A_0 \exp[-(t/\tau)^{\alpha}]$, where A_0 is the pre-exponential factor, α is the stretching parameter, and τ is the characteristic time. From the smooth fitting curves, we could conveniently derive the half lifetime ($t_{1/2}$).

We further carried out nanosecond TA experiments to examine the kinetics of dual-channel charge-transfer reactions of the oxidized dye molecules (D^+) with the photoinjected electrons in titania and the electron-donating species in our electrolyte, which may also impact the EQE height. Employing a dye-grafted titania film infiltrated with an inert electrolyte consisting of 1.0 M 1,3-dimethylimidazolium bis(trifluoromethanesulfonyl)imide (DMITFSI), 50 mM lithium bis(trifluoromethanesulfonyl)imide (LiTFSI), and 1.0 M 4-*tert*-butylpyridine (TBP) in acetonitrile, a control cell was assembled. By recording the transient absorption traces (Fig. 6a) of the control cells, we can derive the half lifetime ($t_{inert}^{1/2}$) of charge recombination between the photoinjected electrons in titania and the holes on the photooxidized dye molecules, being 200 μs for **C265**, which is 7.5 times shorter than that of 1500 μs for **C257**. On the other hand, the addition of the iodine redox couple into the inert electrolyte leads to significantly accelerated absorption decays (Fig. 6b), indicating the hole injection from the photooxidized dye molecules to the redox electrolyte. The half lifetime ($t_{hi}^{1/2}$) of hole injection for **C265** is about 5 μs, over two times smaller than that of 13 μs for **C257**.

It is noted from DFT calculations that for hole injection, the photooxidized state of **C265** has a 10 meV larger change of Gibbs free energy and a 30 meV larger reorganization energy than those of **C257**. As shown in Fig. S13 in ESI,† there is a larger degree of hole delocalization on the conjugated backbone for the photooxidized state of **C257** comapred to **C265**, exerting an adverse effect on the electronic coupling for hole injection. Thereby, it can be postulated that the stronger electronic coupling and the larger driving force for **C265** jointly contribute to its faster hole injection kinetics. Overall, both dyes exhibit close-to-unity hole injection yields (ϕ_{hi}), which are not the governing factor of EQE summits.

We next evaluated photovoltaic parameters by recording the photocurrent density–voltage (j–V) characteristics at an irradiance of 100 mW cm^{-2}, simulated AM1.5 sunlight (Fig. 7a), and the detailed parameters were collected in Table S3, ESI.† The **C265** cell with a smaller energy-gap however exhibits a short-circuit photocurrent density (j_{sc}) of 11.64 mA cm^{-2}, which is notably smaller than that of 16.00 mA cm^{-2} for the **C257** counterpart. Moreover, the anchor variation from BA to CA causes a remarkably decreased open-circuit photovoltage (V_{oc}) from 774 to 694 mV, leading to a markedly lower power conversion efficiency (PCE) of 5.9% for the **C265** cell with respect to that of 8.7% **C257**. We also recorded j–V curves under a series of light irradiances and plotted V_{oc} as a function

of j_{sc} to compare the anchor dependent V_{oc} at a certain j_{sc}. As presented in Fig. 7b, the anchor transformation from BA to CA gives rise to a 76 mV reduction of V_{oc} at a given j_{sc}.

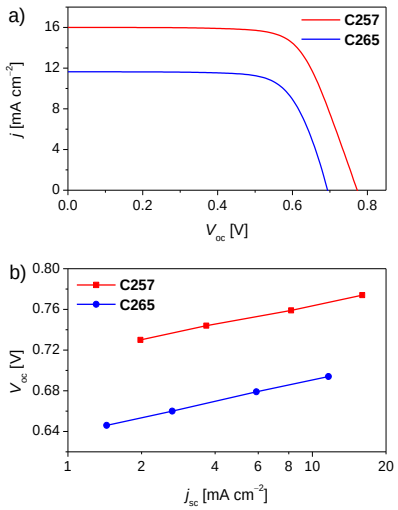

Fig. 7 (a) Current–voltage (j–V) characteristics measured at an irradiance of 100 mW cm^{-2}, simulated AM1.5 sunlight. b) Plots of open-circuit photovoltage (V_{oc}) against short-circuit photocurrent (j_{sc}). An antireflection film was adhered to the testing cells during measurements. The aperture area of the employed metal mask is 0.160 cm^{-2}.

Taking account of the fixed redox electrolyte for cell fabrication, a variation of V_{oc} can be correlated to a movement of the electron quasi-Fermi-level ($\mathbf{E}_{F,n}$) of titania, which results from a shift of titania conduction band edge ($\mathbf{E}_c$) and/or a change of electron density in titania.[44,45] For a given flux of carrier photogeneration, the electron density of titania could be jointly determined by the charge recombination reactions of the photoinjected electrons in titania with the holes localized on the photooxidized dye molecules and the redox electrolyte. Thus, the charge extraction (CE)[46] and transient photovoltage decay (TPD)[47] measurements were further performed to scrutinize the origins of the aforesaid anchor related V_{oc} difference by analyzing the interfacial energetics and kinetics. As depicted in Fig. 8a, the anchor transformation from BA to CA does not bring forth a distinct variation of charges stored in the dye-grafted titania film (Q) at the same potential bias, indicative of a similar conduction-band edge of titania with respect to the electrolyte Fermi-level for these two cells. Hence, the aforementioned inferior photovoltage at a given j_{sc} for the **C265** cell is originated from its over one order of magnitude shorter time constant (τ_e) of charge recombination at a given Q as illustrated in Fig. 8b. In view of the nearly quantitative interception of the photooxidized dye molecules by the iodide anions in our electrolyte discussed in the precedent section, the shorter τ_e of the **C265** cell estimated by TPD mainly reflect faster charge recombination of the titania electrons with the electrolyte oxidative species.

We further probed the microstructure characteristics of the self-assembled dye layer on the planar titania surface by means of X-ray reflectivity (XRR).[48–50] Through fitting reflectivity (R) as a function of perpendicular momentum transfer (Q_z) with a bilayer model (Fig. 8c), we derived the thicknesses (d) and X-ray scattering length density (SLD) of a dye layer on titania made via atomic layer deposition (ALD). A larger SLD of 11.2×10^{-6} Å^{-2} and a decreased d of 1.5 nm are noted for **C265**, in comparison with those of 7.3×10^{-6} Å^{-2} and 2.0 nm for **C257**. Obviously, the distances from the locations of electrons on the surface of titania to those of holes on both triphenylamine and electrolyte are larger for **C257**, giving a basic understanding on the measured charge recombination kinetics.

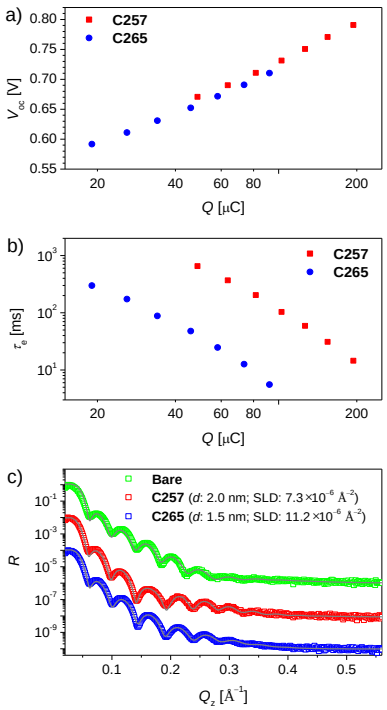

Fig. 8 (a) The relationship of charge stored in the dye-grafted titania film (Q) and open-circuit photovoltage (V_{oc}). (b) Plots of lifetime of photoinjected electrons in titania (τ_e) as a function of charge. (c) Measured (symbols) and simulated (solid lines) XRR curves for the bare and dye-grafted ALD titania films. R is the reflectivity and Q_z is the perpendicular momentum transfer. Each curve is offset by 10^{-2} with respect to the previous one for clarity. The derived thickness (d) and X-ray scattering length density (SLD) of a dye layer on titania are also included in the inset of panel c.

Conclusions

In summary, we have unveiled a picture of stepwise excited state relaxations and multiple state electron injections at the titania/dye interface in triarylamine-based organic dye-sensitized solar cells, based upon ultrafast spectroscopic measurements and theoretical calculations. The gradual excited state energy losses concomitant with multiple torsional relaxations lead to multiexponential electron injection kinetics occurring in a broad time scale from fs to ps, which should be carefully manipulated in the future design of high performance triarylamine-based materials. Our study has again suggested the importance of having long-lived excited states for a narrow energy-gap organic dye with a low-lying LUMO energy level

to suspend the non-electron injecting excited state deexcitation, because a reduced energy offset with respect to titania may often lead to a slower electron injection kinetics. In addition, our work has again enforced that improving the thicknesses of a self-assembled dye layer on titania and keeping the hole locations away from the surface of titania are crucial to attenuate the rate of recombining the photoinjected electrons with the photooxidized dye molecules and redox electrolytes.

Experimental section

Materials

Chlorobenzene, iodine (I_2), lithium iodide (LiI), LiTFSI, and TBP were purchased from Sigma-Aldrich and used without further purification. The scattering TiO_2 paste was purchased from Dyesol and the transparent TiO_2 paste was prepared according to the literature method.[51] **C257**,[32] 1,3-dimethylimidazolium iodide (DMII)[52] and DMITFSI[52] were synthesized according to the literature methods. The details on the synthesis of **C265** are described in ESI.

Computational details

All the calculations were carried out with the Gaussian 09 suite of programs and the 6-311G(d,p) basis set was selected for all of the atoms. To improve the computational efficiency, the long hexyl substituent was reduced to ethyl. Geometry optimizations for the ground state and photooxidized state were performed with the respective hybrid PBE0[53] and UPBE0[54] functionals, which have been previously demonstrated to be appropriate to describe the electronic and optical features of organic donor–acceptor dyes.[55] The exchange-correlation functional CAM-B3LYP[37] was picked to calculate the vertical excitation energies and optimize the geometries of the lowest singlet excited state. The solvent effect on the geometries as well as the transition energies have been taken into account by means of the conductor-like polarizable continuum model (CPCM).[56] The reorganization energies were calculated *via* the equation of $\lambda_{reg}=[\mathbf{E}(M^+)+\mathbf{E}^+(M)]-[\mathbf{E}^+(M^+)+\mathbf{E}(M)]$, where $\mathbf{E}(M^+)$ denotes the energy of a neutral molecule at the optimized geometry of its single-electron oxidized form, $\mathbf{E}^+(M)$ denotes the energy of a oxidized molecule at the optimized geometry of its neutral form, $\mathbf{E}^+(M^+)$ and $\mathbf{E}(M)$ denote the energies of the oxidized and neutral molecules at the optimized geometry of themselves, respectively. Considering the same electrolyte used for these two dyes, the difference of the Gibbs free energy for hole injection were derived from the calculated energy of the lowest unoccupied β orbital.

Voltammetric, UV-Vis, PL, and XRR measurements

Cyclic voltammograms of the dye solutions were recorded on a CHI660C electrochemical workstation and all potentials were reported with respect to the ferrocene/ferrocenium (Fc/Fc^+) reference. Steady-state electronic absorption spectra were recorded on an Agilent G1103A spectrometer. Stationary PL spectra were recorded with an ICCD camera with cw laser excitation at 490 nm. A dyed titania film for electronic absorption and PL measurements was assembled with another bare FTO with a 25-μm-thick Surlyn ring and the internal space was filled with an inert or iodine electrolyte. XRR measurements were carried out with a Bruker D8 discover high-resolution diffractometer by using Cu Kα X-ray radiation (λ=1.542 Å), and the experimental details have been described in our pervious paper.[32]

Dynamic spectroscopic measurements

The same laser source was employed in the fs-TA experiments as outlined in our previous paper.[57] A mode-locked Ti:sapphire laser (Tsunami, Spectra Physics) was used as a source of a regenerative amplifier (RGA, Spitfire, Spectra Physics) to afford 3.7 mJ, 130 fs pulses at 800 nm, which were split into two parts at a ratio of 9/1 with a beam splitter. The main part was delivered to an optical parametric amplifier (TOPAS-C, Light Conversion) to produce pump pulses. The pump light was focused on a rotating sample through a phase-locked chopper. A white light continuum generated by focusing the minor portion of the RGA output on a sapphire was split into two equal beams as the probe and reference lights, which were detected by two multi-channel optical sensors (1024 elements, MS 2022i, CDP Corp.). The polarization between pump and probe beams on a rotating sample was set at the magic angle. The processed signal was displayed with the ExciPRO software (CDP Corp.). All spectra were corrected for the group velocity dispersion of the white light continuum with the Surface Xplorer software (version 2.3) and further analyzed by using the free Glotaran software.[58] The nanosecond TA measurements have been described in our previous paper.[59]

Cell fabrication and characterization

A 9.0+5.0 μm thick, bilayer titania film was coated on a pre-cleaned fluorine-doped tin oxide (FTO) conducting glass (Nippon Sheet Glass, Solar, 4 mm thick) by screen-printing as the negative electrode of DSCs. The size of titania particles is 25 nm for a translucent layer and 350−450 nm for a light-scattering layer. A circular titania electrode (~0.28 cm^2) was dyed by immersing it into a 150 μM dye solution in chlorobenzene for 10 h. The dye-grafted titania electrode was assembled with a platinized FTO electrode by use of a 25-μm-thick Surlyn ring to yield a thin-layer electrochemical cell. The infiltrated iodine electrolyte is composed of 1.0 M DMII, 30 mM I_2, 50 mM LiI, and 1.0 M TBP in acetonitrile. Details on IPCE, *j*–*V*, CE, and TPD measurements can be found in our previous publications.[59,60]

Acknowledgements

We are grateful to the National 973 Program (No. 2011CBA00702), the National 863 Program (No. 2011AA050521), and the National Science Foundation of China (No. 51103146, No. 51125015, and No. 91233206) for financial support.

Notes and references

State Key Laboratory of Polymer Physics and Chemistry, Changchun Institute of Applied Chemistry, Chinese Academy of Sciences, Changchun, 130022, China. Email: peng.wang@ciac.ac.cn; Tel: 0086-431-85262952; Fax: 0086-431-85262953

† *Electronic Supplementary Information (ESI) available: dye synthesis, analyses on anchor dependent energy levels and absorption spectra, and additional data. See DOI: 10.1039/b000000x/*

1 M. Woodhouse and B. A. Parkinson, *Chem. Soc. Rev.*, 2009, **38**, 197–210.
2 A. L. Linsebigler, G. Lu and J. T. Yates, *Chem. Rev.*, 1995, **95**, 735–758.
3 C. McDonagh, C. S. Burke and B. D. MacCraith, *Chem. Rev.*, 2008, **108**, 400–422.
4 N. A. Anderson and T. Lian, *Annu. Rev. Phys. Chem.*, 2005, **56**, 491–519.
5 W. R. Duncan and O. V. Prezhdo, *Annu. Rev. Phys. Chem.*, 2007, **58**, 143–184.
6 B. O'Regan and M. Grätzel, *Nature*, 1991, **353**, 737–740.
7 R. Katoh, A. Furube, A. V. Barzykin, H. Arakawa and M. Tachiya, *Coord. Chem. Rev.*, 2004, **248**, 1195–1213.
8 N. A. Anderson and T. Lian, *Coord. Chem. Rev.*, 2004, **248**, 1231–1246.
9 K. Schwarzburg, R. Ernstorfer, S. Felber and F. Willig, *Coord. Chem. Rev.*, 2004, **248**, 1259–1270.
10 D. F. Watson and G. J. Meyer, *Annu. Rev. Phys. Chem.*, 2005, 56, 119–156.
11 Y. Tachibana, J. E. Moser, M. Grätzel, D. R. Klug and J. R. Durrant, *J. Phys. Chem.*, 1996, **100**, 20056–20062.
12 J. B. Asbury, R. J. Ellingson, H. N. Ghosh, S. Ferrere, A. J. Nozik and T. Lian, *J. Phys. Chem. B*, 1999, **103**, 3110–3119.
13 J. B. Asbury, E. Hao, Y. Wang, H. N. Ghosh and T. Lian, *J. Phys. Chem. B*, 2001, **105**, 4545–4557.
14 G. Benkö, J. Kallioinen, J. E. I. Korppi-Tommola, A. P. Yartsev and V. Sundström, *J. Am. Chem. Soc.*, 2002, **124**, 489–493.
15 D. Kuciauskas, J. E. Monat, R. Villahermosa, H. B. Gray, N. S. Lewis and J. E. McCusker, *J. Phys. Chem. B*, 2002, **106**, 9347–9358.
16 R. Ernstorfer, L. Gundlach, S. Felber, W. Storck, R. Eichberger and F. Willig, *J. Phys. Chem. B*, 2006, **110**, 25383–25391.
17 B. Wenger, M. Grätzel and J.-E. Moser, *J. Am. Chem. Soc.*, 2005, **127**, 12150–12151.
18 A. R. S. Kandada, S. Fantacci, S. Guarnera, D. Polli, G. Lanzani. F. De Angelis and A. Petrozza, *ACS Appl. Mater. Interfaces*, 2013, **5**, 4334–4339.
19 A. Furube, Z.-S. Wang, K. Sunahara, K. Hara, R. Katoh and M. Tachiya, *J. Am. Chem. Soc.*, 2010, **132**, 6614–6615.
20 K. Sunahara, A. Furube, R. Katoh, S. Mori, M. J. Griffith, G. G. Wallace, P. Wagner, D. L. Officer and A. J. Mozer, *J. Phys. Chem. C*, 2011, **115**, 22084–22088.
21 S. Mahanta, A. Furube, H. Matsuzaki, T. N. Murakami and H. Matsumoto, *J. Phys. Chem. C*, 2012, **116**, 20213–20219.
22 M. Juozapavicius, M. Kaucikas, J. J. van Thor and B. C. O'Regan, *J. Phys. Chem. C*, 2013, **117**, 116–123.
23 M. Juozapavicius, M. Kaucikas, S. D. Dimitrov, P. R. F. Barnes, J. J. van Thor and B. C. O'Regan, *J. Phys. Chem. C*, 2013, **117**, 25317–25324.
24 S. A. Haque, E. Palomares, B. M. Cho, A. N. M. Green, N. Hirata, D. R. Klug and J. R. Durrant, *J. Am. Chem. Soc.*, 2005, **127**, 3456–3462.
25 A. Furube, R. Katoh, K. Hara, S. Murata, H. Arakawa and M. Tachiya, *J. Phys. Chem. B*, 2003, **107**, 4162–4166.
26 A. Listorti, B. C. O'Regan and J. R. Durrant, *Chem. Mater.*, 2011, **23**, 3381–3399.
27 C. Martín, M. Ziółek, M. Marchena and A. Douhal, *J. Phys. Chem. C*, 2011, **115**, 23183–23191.
28 M. Ziółek, B. Cohen, X. Yang, L. Sun, M. Paulose, O. K. Varghese, C. A. Grimes and A. Douhal, *Phys. Chem. Chem. Phys.*, 2012, **14**, 2816–2831.
29 Y. Wang, L. Yang, M. Xu, M. Zhang, Y. Cai, R. Li and P. Wang, *J. Phys. Chem. C*, 2014, **118**, DOI: 10.1021/jp410929g.
30 Z. Yao, L. Yang, Y. Cai, C. Yan, M. Zhang, N. Cai, X. Dong and P. Wang, *J. Phys. Chem. C*, 2014, **118**, 2977–2986.
31 Z. Yao, C. Yan, M. Zhang, R. Li, Y. Cai and P. Wang, *Adv. Energy Mater.*, 2014, **4**, DOI: 10.1002/aenm.201400244.
32 M. Zhang, Y. Wang, M. Xu, W. Ma, R. Li and P. Wang, *Energy Environ. Sci.*, 2013, **6**, 2944–2949.
33 J. Franck, *Trans. Faraday Soc.*, 1926, **21**, 536–542.
34 E. Condon, *Phys. Rev.*, 1926, **28**, 1182–1201.
35 J. Clark, T. Nelson, S. Tretiak, G. Cirmi and G. Lanzani, *Nat. Phys.*, 2012, **8**, 225–231.
36 S. Ardo and G. J. Meyer, *Chem. Soc. Rev.*, 2009, **38**, 115–164.
37 T. Yanai, D. P. Tew and N. C. Handy. *Chem. Phys. Lett.*, 2004, **393**, 51–57.
38 C. A. Guido, B. Mennucci, D. Jacquemin and C. Adamo, *Phys. Chem. Chem. Phys.*, 2010, **12**, 8016–8023.
39 T. Nelson, S. Fernandez-Alberti, A. E. Roitberg and S. Tretiak, *Acc. Chem. Res.*, 2014, **47**, 1155–1164.
40 G. Lanzani, M. Nisoli, S. De Silvestri, G. Barbarella, M. Zambianchi and R. Tubino, *Phys. Rev. B*, 1996, **53**, 4453–4457.
41 I. H. M. van Stokkum, D. S. Larsen and R. van Grondelle, *Biochim. Biophys. Acta*, 2004, **1657**, 82–104.
42 R. Berera, C. Herrero, I. H. M. van Stokkum, M. Vengris, G. Kodis, R. E. Palacios, H. van Amerongen, R. van Grondelle, D. Gust, T. A. Moore, A. L. Moore and J. T. M. Kennis, *Proc. Natl. Acad. Sci. USA*, 2006, **103**, 5343–5348.
43 A. V. Ruban, R. Berera, C. Ilioaia, I. H. M. van Stokkum, J. T. M. Kennis, A. A. Pascal, H. van Amerongen, B. Robert, P. Horton and R. van Grondelle, *Nature*, 2007, **450**, 575–578.
44 J. Bisquert, *Phys. Chem. Chem. Phys.*, 2003, **5**, 5360–5364.
45 B. C. O'Regan and J. R. Durrant, *Acc. Chem. Res.*, 2009, **42**, 1799–1808.
46 N. W. Duffy, L. M. Peter, R. M. G. Rajapakse and K. G. U. Wijayant, *Electrochem. Commun.*, 2000, **2**, 658–662.
47 B. C. O'Regan, K. Bakker, J. Kroeze, H. Smit, P. Sommeling and J. R. Durrant, *J. Phys. Chem. B*, 2006, **110**, 17155–17160.
48 S. R. Wasserman, G. M. Whitesides, I. M. Tidswell, B. M. Ocko, P. S. Pershan and J. D. Axe, *J. Am. Chem. Soc.*, 1989, **111**, 5852–5861.
49 G. Decher, *Science*, 1997, **277**, 1232–1237.
50 M. J. Griffith, M. James, G. Triani, P. Wagner, G. G. Wallace and D. L. Officer, *Langmuir*, 2011, **27**, 12944–12950.
51 P. Wang, S. M. Zakeeruddin, P. Comte, R. Charvet, R. Humphry-Baker and M. Grätzel, *J. Phys. Chem. B*, 2003, **107**, 14336–14341.
52 P. Bonhôte, A.-P. Dias, N. Papageorgiou, K. Kalyanasundaram and M. Grätzel, *Inorg. Chem.*, 1996, **35**, 1168–1178.
53 M. Ernzerhof and G. E. Scuseria, *J. Chem. Phys.*, 1999, **110**, 5029–5036.
54 C. Adamo and V. J. Barone, *Chem. Phys.*, 1999, **110**, 6158–6170.

55 D. Jacquemin, E. A. Perpète, G. E. Scuseria, I. Ciofine and C. Adamo, *J. Chem. Theory Comput.*, 2008, **4**, 123–135.

56 M. Cossi, N. Rega, G. Scalmani and V. Barone, *J. Comp. Chem.*, 2003, **24**, 669–681.

57 Y. Wang, L. Yang, J. Zhang, R. Li, M. Zhang and P. Wang, *ChemPhysChem*, 2014, **15**, 1037–1042.

58 J. J. Snellenburg, S. P. Laptenok, R. Seger, K. M. Mullen and I. H. M. van Stokkum, *J. Stat. Softw.*, 2012, **49**, 1–22.

59 J. Liu, R. Li, X. Si, D. Zhou, Y. Shi, Y. Wang and P. Wang, *Energy Environ. Sci.*, 2010, **3**, 1924–1928.

60 N. Cai, Y. Wang, M. Xu, Y. Fan, R. Li, M. Zhang and P. Wang, *Adv. Funct. Mater.*, 2013, **23**, 1846–1854.